THE JOURNAL OF PHYSICAL CHEMISTRY LETTERS
A JOURNAL OF THE AMERICAN CHEMICAL SOCIETY

pubs.acs.org/JPCL

Letter

Hidden Hemibonding in the Aqueous Hydroxyl Radical

Bhaskar Rana and John M. Herbert*

Cite This: *J. Phys. Chem. Lett.* 2021, 12, 8053−8060

Read Online

ACCESS | Metrics & More | Article Recommendations | Supporting Information

ABSTRACT: The existence of a two-center, three-electron hemibond in the first solvation shell of $^{\bullet}$OH(aq) has long been a matter of debate. The hemibond manifests in *ab initio* molecular dynamics simulations as a small-*r* feature in the oxygen radial distribution function (RDF) for $H_2O\cdots{}^{\bullet}OH$, but that feature disappears when semilocal density functionals are replaced with hybrids, suggesting a self-interaction artifact. Using periodic simulations at the PBE0+D3 level, we demonstrate that the hemibond is actually still present (as evidenced by delocalization of the spin density) but is obscured by the hydrogen-bonded feature in the RDF due to a slight elongation of the hemibond. Computed electronic spectra for $^{\bullet}$OH(aq) are in excellent agreement with experiment and confirm that hemibond-like configurations play an outsized role in the spectroscopy due to an intense charge-transfer transition that is strongly attenuated in hydrogen-bonded configurations. Apparently, 25% exact exchange (as in PBE0) is insufficient to eliminate delocalization of unpaired spins.

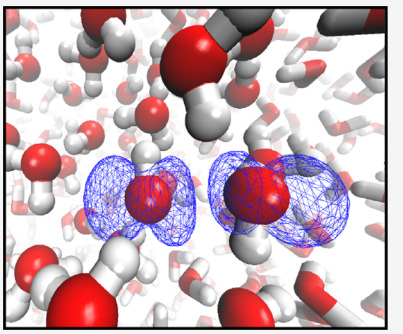

First described by Pauling,[1] a two-center, three-electron (2c−3e) "hemibond" is formed when a doubly occupied frontier orbital of one molecule overlaps favorably with the half-filled orbital of a radical, resulting in a stabilizing interaction with a bond order of 1/2. Computational evidence for the existence of hemibonds has been put forward in a variety of systems,[2−8] and hemibonding has long been discussed in the context of aqueous-phase pulse radiolysis experiments involving sulfur-containing species.[9−12] Definitive experimental evidence for hemibonds exists only in a few cases, however, including $(H_2S)_n^+$,[13,14] $(CH_3SH)_2^+$,[15] $(CH_3S)_2^+$,[16] $[(CH_3)_2S]_2^+$,[17] Cl···NH_3,[18] and a few other systems.[19,20]

Hemibonding in $^{\bullet}$OH(aq) was predicted in some of the earliest *ab initio* molecular dynamics (*ai*MD) simulations using density functional theory (DFT),[21−25] but these predictions were quickly rejected as artifacts of self-interaction error (SIE) associated with the use of semilocal functionals,[25] since SIE is known to overstabilize 2c−3e bonds.[26,27] More recently, it has been suggested that the hemibonds observed in those early simulations might instead be artifacts of a too-small periodic simulation cell.[28−31] Perhaps for these reasons, the possibility of a hemibonded solvation motif does not seem to have been considered in the recent analysis of ultrafast X-ray experiments on $^{\bullet}$OH(aq).[32] The latest *ai*MD simulations using hybrid functionals report no evidence of the feature traditionally associated with this motif,[33−35] namely, a peak at 2.2−2.3 Å in the radial distribution function (RDF) for oxygen.[25] In the present work, we use periodic DFT simulations at the PBE0+D3 level[36,37] to demonstrate that the disappearance of this feature in hybrid DFT does not imply the absence of a hemibonded solvation motif. In contrast to what has become conventional wisdom, spin delocalization persists even in the presence of 25% exact exchange. For $^{\bullet}$OH(aq), hemibond-like configurations prove to be crucial in explaining the electronic absorption spectroscopy.

In an effort to avoid artifacts arising from *ai*MD in small simulation cells, we recently reported mixed quantum mechanics/molecular mechanics (QM/MM) simulations of $^{\bullet}$OH(aq) in very large unit cells.[38] Figure 1a reproduces the O*···O RDFs from these simulations, where O* denotes the oxygen atom of the radical. The appearance or disappearance of a feature at $r_{O^*O} \approx 2.2-2.3$ Å is usually equated with the presence or absence of hemibonding,[25,28,31,33,39] and this feature vanishes when semilocal functionals are replaced by hybrids,[33] or when a self-interaction correction is introduced.[25,39] Our QM/MM results are more ambiguous,[38] and reveal that the feature at small r_{O^*O} is quite sensitive to the fraction of exact exchange, diminishing in prominence when BLYP is replaced by functionals such as B3LYP or PBE0, and vanishing altogether for the BH&HLYP functional that contains 50% exact exchange. On the other hand, while these QM/MM simulations used a very large periodic simulation cell (1024 water molecules), the QM region was limited to $OH(H_2O)_{31}$, and the simulation time scale was restricted to <5 ps because exchange of QM and MM water molecules in the cybotactic region takes place on a time scale of only a few picoseconds.[38]

While the prevailing viewpoint in the literature is that the hemibonded solvation motif is an artifact, calculations on small

Received: July 15, 2021
Accepted: August 13, 2021

https://doi.org/10.1021/acs.jpclett.1c02283
J. Phys. Chem. Lett. 2021, 12, 8053−8060

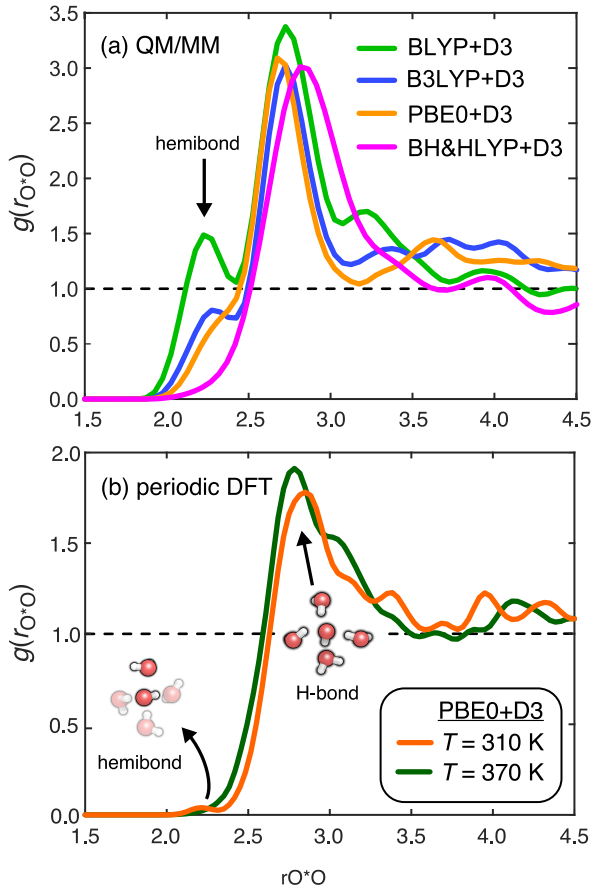

Figure 1. RDFs for O*···O, where O* denotes the hydroxyl oxygen, computed from (a) QM/MM simulations at T = 300 K using three different functionals, versus (b) periodic *ai*MD simulations at the PBE0+D3 level, performed at either of two temperatures. Data in (a) are from ref 38.

$^{\bullet}OH(H_2O)_n$ clusters suggest that hemibonded configurations are needed to explain the electronic absorption spectrum of $^{\bullet}OH(aq)$.[40−44] The band maximum of that spectrum appears at 230 nm (5.4 eV),[45−50] which constitutes an enormous blue-shift compared to the $\tilde{A}^2\Sigma^+ \leftarrow \tilde{X}^2\Pi$ transition of gas-phase $^{\bullet}OH$, which appears at 307 nm (4.0 eV).[51,52] It is suggested[42] that the 230 nm transition does not involve the $\tilde{A}^2\Sigma^+$ state of the radical at all, but instead arises due to an intense $1b_2(H_2O) \rightarrow 2p(^{\bullet}OH)$ charge-transfer transition, specifically associated with hemibonded configurations. Our QM/MM simulations seemed to confirm this mechanism.[38] In summary, the situation is that scant attention has been paid to hemibonded configurations in condensed-phase *ai*MD simulations because they were thought to be artifacts, yet these "artifacts" (or perhaps rare events or a minority population) seem to be necessary to reproduce the ultraviolet (UV) spectroscopy of $^{\bullet}OH(aq)$.

To further investigate this issue, we performed *ai*MD simulations of $^{\bullet}OH(aq)$ using periodic DFT, in a unit cell $[OH(H_2O)_{63}]$ that is thought to be large enough to avoid finite-size artifacts.[28,31] One simulation employs the PBE0+D3 functional at T = 370 K, consistent with the most recent hybrid DFT *ai*MD simulations of $^{\bullet}OH(aq)$,[34] except that the unit cell is twice as large in the present work. (Simulation details can be found in section S1 of the Supporting Information.) Historically, *ai*MD simulations of liquid water using semilocal density functionals have been run at elevated temperature (often T = 350 K) to simulate the properties of the liquid at T = 298 K, which is an effort to counteract the fact that the liquid predicted by semilocal functionals is overstructured and glassy.[53] At the PBE0+D3 level, however, it is not clear that the use of an elevated temperature is warranted,[54] so we also performed simulations at T = 310 K. The normal freezing temperature of PBE0+D3 water has recently been determined to be T = 268 K,[55] so both of our thermodynamic state points lie within the liquid regime.

Figure 1b compares the O*···O RDFs obtained from our periodic DFT simulations. RDFs are computed using structures from the post-equilibration part of the trajectories, sampled every 50 fs and binned by using Δr = 0.017 Å. RDFs obtained at T = 310 K and T = 370 K are qualitatively similar, with the main peak at r_{O^*O} = 2.8−2.9 Å as compared to r_{O^*O} = 2.7 Å in QM/MM simulations using the same functional. The feature at smaller values of r_{O^*O} that is typically associated with the hemibond is absent from the periodic simulation at T = 370 K, consistent with previous simulations at the same temperature but using a smaller unit cell.[34] At T = 310 K, however, one can just barely observe the appearance of a feature at r_{O^*O} = 2.2 Å. Even at the higher temperature, the RDF is not zero at r_{O^*O} = 2.2 Å although there is no distinct feature prior to the main hydrogen-bonding peak.

To understand the discrepancies between the periodic DFT simulations reported here and the periodic QM/MM simulations reported previously,[38] we performed a QM/MM simulation on a large spherical droplet, with a central $OH(H_2O)_{64}$ region described at the PBE0 + D3/6-31G* level. The O*···O RDF from this trajectory (Figure S2a) resembles the periodic ones in Figure 1b much more closely than do the periodic QM/MM results in Figure 1a, where the QM region is $OH(H_2O)_{31}$. This indicates that finite QM size effects in QM/MM simulations can have just as significant of an impact as SIE artifacts or finite unit cell size.

In view of the close association of the small-r_{O^*O} peak with the hemibond, it is easy to see how one might conclude from the T = 370 K data in Figure 1b that the hemibond is absent in these simulations. Semilocal functionals such as BLYP produce a much more pronounced feature, closer to the BLYP+D3 result obtained from QM/MM simulations (Figure 1a). This leaves open the possibility that the hemibond could be a rare event or a transient fluctuation. However, the appearance of a small-r_{O^*O} feature at lower temperature suggests that the hemibond instead corresponds to a local minimum on the potential energy surface or an "inherent structure".[56] We will return to this issue below.

Semilocal DFT simulations, using the same $OH(H_2O)_{63}$ simulation cell that is employed herein, suggest that the hemibonded $H_2O\cdots{}^{\bullet}OH$ motif is an alternative structure that lies 2−3 kcal/mol higher in energy than the hydrogen-bonded structure $HOH\cdots{}^{\bullet}OH$.[31] In contrast, exhaustive search of the $^{\bullet}OH(H_2O)_7$ potential energy surface at the level of second-order Møller−Plesset perturbation theory (MP2) suggests that the global minimum structure at that particular cluster size exhibits a hemibond.[57] Although this observation may not be relevant to $^{\bullet}OH(aq)$, insofar as the hydroxyl radical sits at the periphery of the $^{\bullet}OH(H_2O)_7$ cluster, it is significant that a hemibonded minimum-energy structure can be found at a level of theory that is rigorously free of SIE. If hemibonded

https://doi.org/10.1021/acs.jpclett.1c02283
J. Phys. Chem. Lett. 2021, 12, 8053−8060

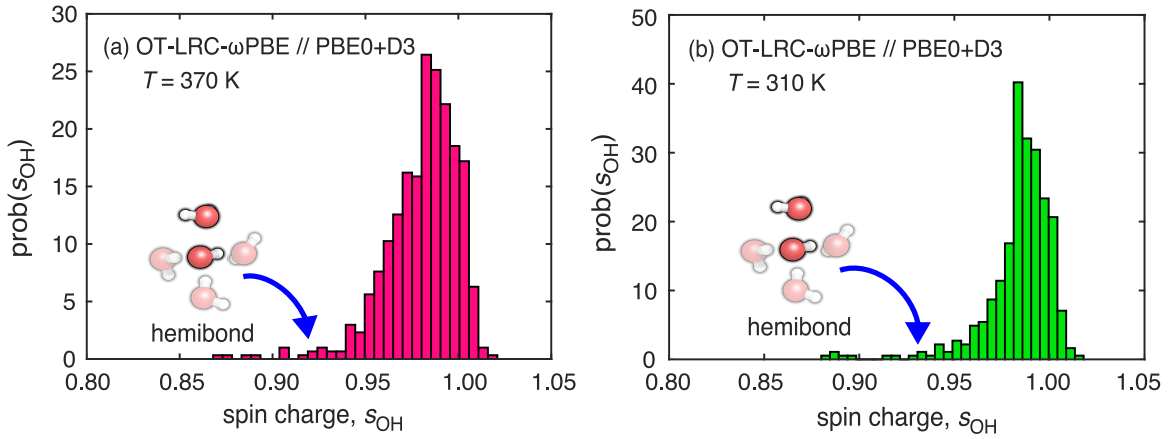

Figure 2. Histograms of the total spin charge s_{OH} on the •OH moiety, for configurations obtained from periodic PBE0+D3 simulations at (a) T = 370 K vs (b) T = 310 K. The charges themselves were computed at the OT-LRC-ωPBE/6-31++G* level (using $\omega = 0.398a_0^{-1}$), which is the same level of theory that was used previously to determine spin leakage in QM/MM simulations.[38]

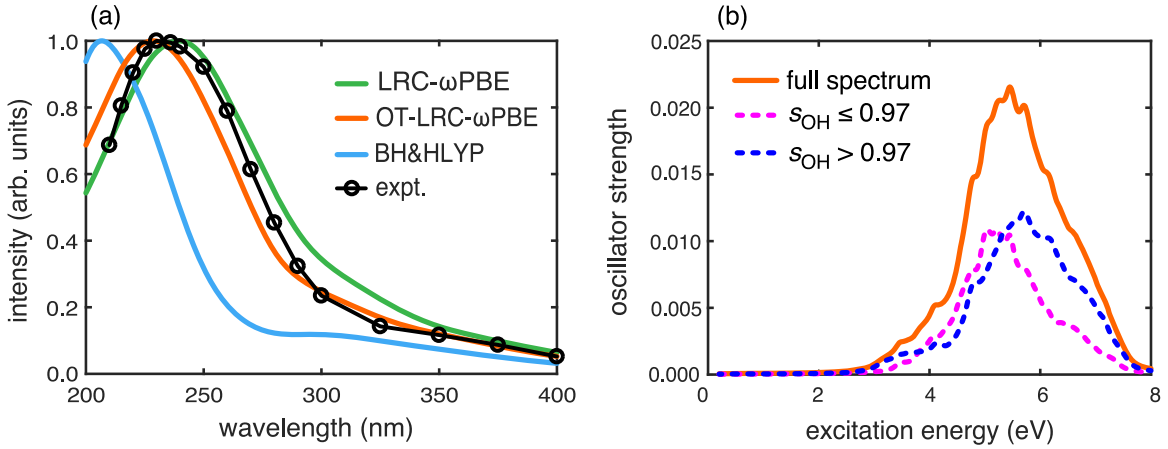

Figure 3. Simulated TD-DFT absorption spectra of •OH(aq) at T = 370 K for an ensemble of structures obtained from a periodic PBE0+D3 simulation. (a) Comparison of spectra obtained by using various functionals (6-31++G* basis set) vs experimental data corresponding to extinction coefficients measured at 25 °C.[50] All spectra are separately normalized to unit intensity at their respective maxima. (b) OT-LRC-ωPBE spectrum decomposed into separate contributions from spin-localized configurations of the radical ($s_{OH} > 0.97$) vs hemibonded configurations that exhibit spin leakage ($s_{OH} \le 0.97$). TD-DFT spectra in (a) have been smoothed using Gaussian windowing whereas the ones in (b) have not been.

configurations in •OH(aq) are indeed rare, as suggested by the condensed-phase results in ref 31, and especially if hybrid functional increase the O*···O distance relative to what is obtained by using semilocal functionals, then it is easy to see how a distinct hemibonding feature in $g(r_{O^*O})$ might be hidden beneath the much larger hydrogen-bonded feature, especially in warmer water.

To obtain more detail about the local solvation environment around •OH(aq), we computed the probability distribution for the number of hydrogen bonds (n_{HB}) in the first solvation shell of the radical (Figure S3), using standard geometry-dependent cutoffs to define a hydrogen bond.[38,58] The average value is $\langle n_{HB} \rangle \approx 2$, including both donor and acceptor hydrogen bonds, which represents under-coordination relative to the canonical hydrogen-bonded structure that is shown in Figure 1b. This soft first-shell structure is in agreement with previous QM/MM simulations using the long-range corrected (LRC) functional LRC-ωPBE+D3,[38] and with periodic simulations using self-interaction-corrected functionals.[25,39]

Because of the apparent overlap between features in $g(r_{O^*O})$ that represent hydrogen-bonded versus hemibonded solvation motifs, we turn to an electronic definition of the hemibond based upon spin delocalization (or "spin leakage") from the radical to the first-shell water molecules. We have previously used such a metric to infer the existence of hemibonded configurations in QM/MM simulations,[38] by defining the "spin charge" s_{OH} to be the sum of Mulliken charges on the radical, computed by using the spin density $\rho_\alpha - \rho_\beta$. The value of s_{OH} can distinguish hemibonding from hydrogen bonding, even if the former is a rare event, because the hemibond owes its existence to favorable overlap between the half-occupied O*(2p) orbital and a lone pair orbital of a nearby water molecule, leading to spin leakage upon formation of the 2c−3e bond.

Figure 2 presents one-dimensional probability distribution for s_{OH} obtained from the periodic DFT trajectories. To make contact with our previous QM/MM simulations,[38] where we quantified the values of s_{OH} that correspond to hemibonding, we compute the Mulliken charges at the "optimally tuned" (OT)-LRC-ωPBE/6-31++G* level (as described in the Supporting Information) using 600 structures obtained from the *ai*MD simulations, each separated in time by 25 fs. The resulting ensemble of s_{OH} values is peaked just below 1.0, at either simulation temperature, indicating nearly complete

https://doi.org/10.1021/acs.jpclett.1c02283
J. Phys. Chem. Lett. 2021, 12, 8053−8060

localization of the unpaired spin. Nevertheless, the distribution exhibits a long tail stretching to about 0.85 in electron charge units. This tail arises from spin leakage in certain configurations and indicates the presence of some hemibonding. In view of this tail, the existence of some structures with smaller values of r_{O^*O} (as compared to the canonical hydrogen-bonded value, $r_{O^*O} \approx 2.8$ Å) is unsurprising; we have previously shown that the O*···O distance is inversely correlated to the extent of spin leakage.[38] The s_{OH} probability distributions obtained from periodic PBE0+D3 simulations most closely resemble QM/MM results using LRC-ωPBE+D3. In those particular QM/MM simulations, the small-r_{O^*O} feature in $g(r_{O^*O})$ was absent, just as it is for the periodic PBE0+D3 simulations reported here.

In addition to questions about structure, there exists a discussion regarding the origin of the UV spectrum of $^{\bullet}$OH(aq).[38,40−42,44] It has been suggested that hemibonded configurations are needed to explain the main feature in the aqueous-phase spectrum, which appears at $\lambda \approx 230$ nm[45−50] and is therefore significantly shifted relative to the gas-phase absorption at $\lambda = 307$ nm.[51,52] The present state of understanding is that the weak $\tilde{A}^2\Sigma^+(\sigma_{lp}^2\sigma_b^1\pi^4) \leftarrow \tilde{X}^2\Pi(\sigma_{lp}^2\sigma_b^2\pi^3)$ transition[41] that is responsible for the gas-phase spectrum is overwhelmed in solution by a charge-transfer transition with a much larger oscillator strength, which is present in hemibonded configurations (where the O*···O distance is relatively short) but is quenched in hydrogen-bonded configurations where r_{O^*O} is larger. Even if the hemibond is a minority species, it may yet have an outsized role in the spectroscopy of $^{\bullet}$OH(aq).[38,41,42] Note also that the degeneracy of the $^2\Pi$ ground state of gas-phase $^{\bullet}$OH is lifted in solution. This splitting is 0.5−0.6 eV in our calculations (consistent with cluster results[40]) and therefore does not affect the UV spectroscopy of the radical, but is also not discernibly different in hemibonded vs hydrogen-bonded configurations.

Figure 3a presents absorption spectra of $^{\bullet}$OH(aq) computed by using time-dependent (TD-)DFT with three different functionals, for an ensemble of structures obtained from the periodic PBE0+D3 simulations at $T = 370$ K. These calculations employ the protocol developed in ref 38, and details are provided in the Supporting Information. The three functionals that are used (BH&HLYP, LRC-ωPBE, and OT-LRC-ωPBE) each afford reasonable results for this system in QM/MM simulations.[38] Figure 3a is plotted in wavelength units, and the corresponding spectra in energy units can be found in Figure S4, with band maxima listed in Table S1.

Spectra computed using LRC-ωPBE and OT-LRC-ωPBE are in excellent agreement with experiment, in terms of both the band shape and the position of λ_{max}. For the OT functional, in particular, the band maximum differs from experiment by <0.1 eV, which is insignificant compared to the effect of vibrations on the vertical excitation spectrum.[59] (These are described here by means of classical sampling.) Such a difference is also small in comparison to typical basis-set effects in TD-DFT excitation energies.[60] The band maximum of the spectrum computed with LRC-ωPBE is red-shifted by 0.25 eV with respect to experiment but overall is still a reasonable match, whereas the TD-BH&HLYP result is significantly blue-shifted (by 0.6 eV). This is not unusual for functionals that contain such a large fraction of exact exchange.[61]

The use of LRC functionals in aqueous-phase TD-DFT calculations is necessary to avoid contamination of the spectrum by a plethora of spurious, low-energy charge-transfer states.[62−65] The presence of such states adds considerably to the cost of the calculation but can also impact line shapes, via spurious intensity borrowing.[62] Functionals such as BH&HLYP with a larger-than-normal fraction of exact exchange have also been used to address this problem,[66] but they tend to overestimate valence excitation energies, pushing them closer to Hartree−Fock values that are typically overestimated by 0.8 eV or more.[61] LRC functionals also have a tendency to overestimate valence excitation energies, as compared to functionals such as B3LYP or PBE0 with 20−25% exact exchange, but to a lesser extent as compared to BH&HLYP.[61] These are general observations based on benchmark statistical assessments, but they hold perfectly for the present system.

To investigate the specific role of hemibonded configurations in the absorption spectrum of $^{\bullet}$OH(aq), we will ultimately partition the spectrum into separate contributions from hemibonded and non-hemibonded configurations, according to the value of s_{OH}. As a prelude to that analysis, we first examine joint probability distributions of s_{OH} with r_{O^*O} and with $\max_n\{f_{0,n}\}$, meaning the maximum oscillator strength $f_{0,n}$ that is obtained for any of the $|0\rangle \rightarrow |n\rangle$ transitions in the low-energy part of the TD-DFT spectrum. These joint probability distributions are plotted in Figure 4 and allow us to choose a cutoff value of s_{OH} for use in the spectral decomposition.

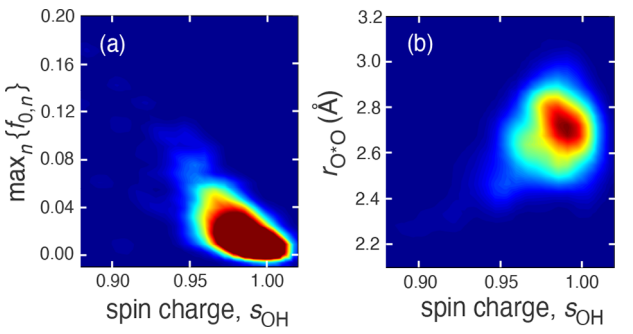

Figure 4. Joint probability distributions of s_{OH} together with (a) $\max_n\{f_{0,n}\}$ and (b) r_{O^*O}, for the periodic PBE0 + D3 trajectory at T = 370 K.

The joint probability distribution in (s_{OH}, $\max_n\{f_{0,n}\}$) is depicted in Figure 4a for the trajectory at $T = 370$ K. The main feature appears at $s_{OH} \approx 1.0$, indicating spin localization and thus hydrogen bonding. That said, the long tail in the distribution of s_{OH} is associated with the largest oscillator strengths in the TD-DFT calculations. Values of s_{OH} and $\max_n\{f_{0,n}\}$ are anticorrelated, with oscillator strengths in the tail of the s_{OH} distribution that are 4−5 times larger than those obtained for hydrogen-bonded configurations.

Figure 4b shows the joint probability distribution in (s_{OH}, r_{O^*O}), where r_{O^*O} is the distance from O* to the nearest water oxygen. Values $r_{O^*O} < 2.5$ Å are expected for hemibonded configurations, and these smaller values do indeed correlate with spin leakage, as measured by s_{OH}. On the basis of these joint probability distributions, we selected a cutoff value of $s_{OH} = 0.97$ to define the hemibonded configurations. Figures S5 and S6 examine one- and two-coordinate probability

https://doi.org/10.1021/acs.jpclett.1c02283
J. Phys. Chem. Lett. 2021, 12, 8053−8060

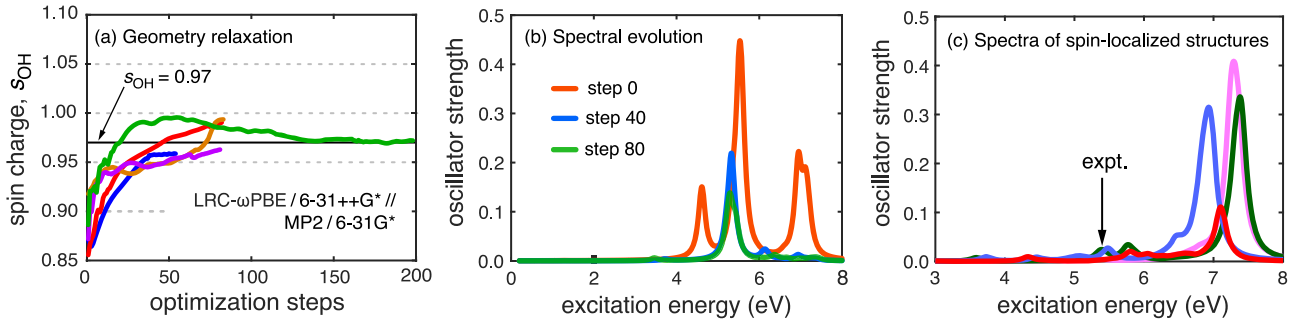

Figure 5. Results from cluster geometry relaxations at the MP2/6-31G* level. (a) Spin charge s_{OH}, computed at the OT-LRC-ωPBE/6-31++G* level, as hemibonded structures extracted from a periodic PBE0+D3 simulation are relaxed at the MP2 level. (b) TD-DFT spectra at various steps along the MP2 relaxation trajectory of one particular cluster, corresponding to structure "D" in Figures S11 and S12. Spectra were computed at the LRC-ωPBE/6-31++G* level with $\omega = 0.398a_0^{-1}$. Several other examples, corresponding to the structure relaxations shown in (a), can be found in Figure S12. (c) TD-DFT spectra for several spin-localized (non-hemibonded) snapshots, for which $s_{OH} \approx 1.00$.

distributions for the geometric parameters that have previously been used to define the hemibond (r_{O^*O} and two angles).[38,42] One-dimensional probability distributions (Figure S5) are similar to what we obtained in QM/MM simulations using the LRC-ωPBE+D3 functional, and the joint probability distributions (Figure S6) demonstrate that geometric definitions of the hemibond agree with the electronic definition based on s_{OH}. In other words, a hemibond in the traditional sense was present all along in periodic *ai*MD simulations based on hybrid functionals, but was been overlooked because it does not give rise to the distinct feature in $g(r_{O^*O})$ that has previously been assumed to be the hallmark of hemibonded $^\bullet$OH(aq). From QM/MM simulations using a variety of density functionals, we know that the average O*···O distance associated with hemibonding shifts to slightly larger values of r_{O^*O} as the fraction of exact exchange is increased (see Table S2). This is how the hemibonded radical manages to hide beneath the larger hydrogen-bonded feature in the RDF, in *ai*MD simulations using hybrid functionals.

Of the snapshots used to generate the absorption spectra in Figure 3a, only 25% satisfy the criterion $s_{OH} \leq 0.97$. However, this minority population cannot be ignored when it comes to the UV spectroscopy, as it supports an intense $1b_2(H_2O) \rightarrow 2p(^\bullet OH)$ charge-transfer transition. As a result, the 25% population of hemibonded radicals contributes about equally to the absorption spectrum alongside the 75% of spin-localized configurations, as shown in the spectral decomposition presented in Figure 3b. The disproportionate contribution from hemibonded configurations is a direct result of the 4−5 times larger oscillator strengths associated with these geometries, which can be seen clearly in Figure S7 where the total oscillator strength is partitioned according to s_{OH}. Whereas the decomposition in Figure 3b is weighted by population, Figure S7 makes it clear that the overwhelming majority of the integrated oscillator strength comes from hemibonded configurations.

To investigate whether the hemibonded structures in the periodic PBE0+D3 simulations represent transient fluctuations or genuine inherent structures, we selected several snapshots from different parts of the s_{OH} distribution and then quenched (optimized) these structures in nonperiodic calculations, including all water molecules within 5.5 Å around the radical and using dielectric continuum boundary conditions.[67] Results of these PBE0+D3/6-31G* optimizations (Figures S8 and S9) do not suggest any consistent outcome to these quenches; configurations that start off hemibonded ($s_{OH} < 0.95$) sometimes spin-localize upon optimization, but in other cases structures that are not initially hemibonded begin to exhibit spin leakage when quenched. This suggests that there are indeed local minima that correspond to hemibonded solvation motifs, at the PBE0+D3 level of theory.

To ascertain whether these hemibonded minima might simply be SIE artifacts, additional cluster optimizations with larger QM regions were performed at the MP2/6-31G* level (Figure S10), including all water molecules within 7.2 Å of the radical. In all cases where the starting geometry exhibits a hemibond, the Hartree−Fock spin density fully localizes onto the hydroxyl moiety during MP2 optimization, as shown in Figure 5a, suggesting that the spin delocalization is indeed an artifact. Closer examination, however, reveals that the hemibonded water moves slightly farther away from the radical upon MP2 structural relaxation (Figure S11a) yet maintains a *pseudo-hemibond* configuration, by which we mean that an exposed O*···O facet persists with no intervening hydrogen bond. The O*···O distance in these pseudo-hemibonded structures is larger than what is traditionally associated with a hemibond, and there is no spin delocalization. The latter observation makes sense in view of the decreased orbital overlap at larger distance.

Having suggested that spin-delocalized DFT hemibonds play an important role in rationalizing the experimental UV spectrum, what does this new observation of spin-localization at the MP2 level say about the UV spectroscopy of $^\bullet$OH(aq)? To answer this question, we turn to hemibonded dimer and pentamer cluster models, for which we have computed absorption spectra by varying the distance between the hydroxyl moiety and the neighboring water molecules, leaving the exposed O*···O facet in place. The evolution of various properties as a function of r_{O^*O} is shown in Tables S3 and S4. The spin charge rapidly localizes onto the radical as the O*···O distance increases, yet the most intense feature in the electronic spectrum remains a charge-transfer transition from a water molecule that is *pseudo-hemibonded* to the radical, even for $r_{O^*O} = 3.4$ Å where spin localization is complete. The presence of several additional water molecules in the case of $^\bullet OH(H_2O)_4$ does not alter this observation.

Finally, we computed TD-DFT absorption spectra along the MP2 geometry relaxation pathways that were discussed above, to observe how gradual spin localization affects the UV spectrum. One such example is shown in Figure 5b, and

https://doi.org/10.1021/acs.jpclett.1c02283
J. Phys. Chem. Lett. 2021, 12, 8053−8060

additional examples can be found in Figure S12. As in the dimer and pentamer models, the most intense transition remains the $1b_2(H_2O) \rightarrow 2p(^{\bullet}OH)$ charge-transfer transition, even for O*···O distances large enough to engender complete spin localization. (Representative attachment and detachment densities for this charge-transfer transition are shown in Figure S13.) Although the intensity of this feature is reduced as the spin localizes onto the $^{\bullet}OH$ moiety, spectra computed at non-hemibonded configurations do not exhibit any comparable transition in the region of the experimental λ_{max} for $^{\bullet}OH(aq)$, as shown in Figure 5c.

We take this to mean that although no spin-delocalized hemibond seems to exist for $^{\bullet}OH(aq)$ at the MP2 level (in any sense that Pauling would likely recognize as such),[1] any transient fluctuation into a pseudo-hemibonded $HO^{\bullet}\cdots OH_2$ geometry exhibits a $1b_2(H_2O) \rightarrow 2p(^{\bullet}OH)$ excitation consistent with the experimental UV spectrum of $^{\bullet}OH(aq)$, even for O*···O distances considerably larger than those typically associated with hemibonding. Shorter O*···O distances may be stabilized by SIE, but this is not required to obtain the $1b_2(H_2O) \rightarrow 2p(^{\bullet}OH)$ charge-transfer transition. In hindsight, a significant fraction of the snapshots tagged as "non-hemibonded" (based on a spin-charge cutoff) in the spectral decomposition of Figure 3b could likely be categorized as pseudo-hemibonded.

In summary, careful analysis of periodic PBE0+D3 simulations of $^{\bullet}OH(aq)$ upends the conventional view that hemibonding disappears when hybrid functionals are employed. A distinctive feature in $g(r_{O^*O})$ does indeed disappear in warmer water, only to re-emerge upon cooling to T = 310 K, but hemibonded configurations persist even at T = 370 K, where they hide in plain sight beneath a much larger hydrogen-bonded feature in $g(r_{O^*O})$. Structural quenches of the periodic PBE0+D3 trajectories suggest that the hemibond is an inherent structure at this level of theory. When the same structures are relaxed at the (SIE-free) MP2 level of theory, the unpaired spin localizes on the hydroxyl moiety and thus the traditional 2c−3e hemibond disappears, yet a "pseudo-hemibond" persists, characterized by an O*···O close contact with no intervening hydrogen bond. This appears to be enough to facilitate an intense $1b_2(H_2O) \rightarrow 2p(^{\bullet}OH)$ charge-transfer transition at an excitation energy that is consistent with the experimental UV spectrum of $^{\bullet}OH(aq)$. No electronic transitions that are consistent with experiment can be found in hydrogen-bonded geometries.

A broader implication of this work is that it adds to the understanding that spin delocalization from a radical to its surroundings need not disappear when standard hybrid functionals with 20−25% exact exchange are employed. This has implications for the description of unpaired spins in other contexts, such as polarons in solid-state semiconductors, where (de)localization of charge carriers or other spin defects is sensitive to the fraction of exact exchange.[68−75] It is sometimes assumed that functionals such as B3LYP or PBE0 will localize a hole, but that assumption has been demonstrated to fail in some cases,[69−72] as it does for $^{\bullet}OH(aq)$.

■ ASSOCIATED CONTENT

Supporting Information

The Supporting Information is available free of charge at https://pubs.acs.org/doi/10.1021/acs.jpclett.1c02283.

Details of the simulations and other calculations along with additional analysis (PDF)

■ AUTHOR INFORMATION

Corresponding Author

John M. Herbert − *Department of Chemistry and Biochemistry, The Ohio State University, Columbus, Ohio 43210, United States;* orcid.org/0000-0002-1663-2278; Email: herbert@chemistry.ohio-state.edu

Author

Bhaskar Rana − *Department of Chemistry and Biochemistry, The Ohio State University, Columbus, Ohio 43210, United States;* orcid.org/0000-0002-8751-7314

Complete contact information is available at: https://pubs.acs.org/10.1021/acs.jpclett.1c02283

Notes

The authors declare the following competing financial interest(s): J.M.H. serves on the board of directors of Q-Chem Inc.

■ ACKNOWLEDGMENTS

This work was supported by National Science Foundation Grant CHE-1955282. Calculations were performed at the Ohio Supercomputer Center under Project PAA-0003.[76] We thank Dr. Kevin Carter-Fenk for help compiling and running CP2K.

■ REFERENCES

(1) Pauling, L. The nature of the chemical bond. III. The one-electron bond and the three-electron bond. *J. Am. Chem. Soc.* **1931**, *53*, 3225−3237.

(2) Gill, P. M. W.; Radom, L. Structures and stabilities of singly charged three-electron hemibonded systems and their hydrogen-bonded isomers. *J. Am. Chem. Soc.* **1988**, *110*, 4931−4941.

(3) Fourrè, I.; Bergés, J. Structural and topological characterization of the three-electron bond: The SO radicals. *J. Phys. Chem. A* **2004**, *108*, 898−906.

(4) Pan, P.-R.; Lin, Y.-S.; Tsai, M.-K.; Kuo, J.-L.; Chai, J.-D. Assessment of density functional approximations for the hemibonded structure of the water dimer radical cation. *Phys. Chem. Chem. Phys.* **2012**, *14*, 10705−10712.

(5) Tsai, M.-K.; Kuo, J.-L.; Lu, J.-M. The dynamics and spectroscopic fingerprint of hydroxyl radical generation through water dimer ionization: *Ab initio* molecular dynamic simulation study. *Phys. Chem. Chem. Phys.* **2012**, *14*, 13402−13408.

(6) Lu, E.-P.; Pan, P.-R.; Li, Y.-C.; Tsai, M.-K.; Kuo, J.-L. Structural evolution and solvation of the OH radical in ionized water radical cations $(H_2O)_n^+$, n = 5−8. *Phys. Chem. Chem. Phys.* **2014**, *16*, 18888−18895.

(7) Do, H.; Besley, N. A. Structure and bonding in ionized water clusters. *J. Phys. Chem. A* **2013**, *117*, 5385−5391.

(8) Do, H.; Besley, N. A. Proton transfer or hemibonding? The structure and stability of radical cation clusters. *Phys. Chem. Chem. Phys.* **2013**, *15*, 16214−16219.

(9) Asmus, K.-D. Stabilization of oxidized sulfur centers in organic sulfides. Radical cations and odd-electron sulfur−sulfur bonds. *Acc. Chem. Res.* **1979**, *12*, 436−442.

(10) Chaudhri, S. A.; Asmus, K.-D. Experimental evidence of the $[H_2SSH_2]^+$ radical cation in solution. *Angew. Chem., Int. Ed. Engl.* **1981**, *20*, 672−673.

(11) Mönig, J.; Goslich, R.; Asmus, K.-D. Thermodynamics of S∴S $2\sigma/1\sigma^*$ three-electron bonds and deprotonation kinetics of thioether

radical cations in aqueous solution. *Ber. Bunsenges. Phys. Chem.* **1986**, *90*, 115−121.
(12) Asmus, K.-D. Sulfur-centered three-electron bonded radical species. In *Sulfur-Centered Reactive Intermediates in Chemistry and Biology*; Chatgilialoglu, C., Asmus, K.-D., Eds.; Plenum Press: New York, 1990; Vol. *197*, pp 155−172.
(13) Wang, D.; Fujii, A. Spectroscopic observation of two-center three-electron bonded (hemi-bonded) structures of $(H_2S)_n^+$clusters in the gas phase. *Chem. Sci.* **2017**, *8*, 2667−2670; *Erratum: Chem. Sci.* **2018**, *9*, 3893−3894.
(14) Wang, D.; Hattori, K.; Fujii, A. The S ∴π hemibond and its competition with the S ∴S hemibond in the simplest model system: Infrared spectroscopy of the $[\text{benzene-}(H_2S)_n]^+$ (n = 1−4) radical cation clusters. *Chem. Sci.* **2019**, *10*, 7260−7268.
(15) Illies, A. J.; Livant, P.; McKee, M. L. Association of dimethyl sulfide radical cation with dimethyl sulfide. Strength of a two-center three-electron bond. *J. Am. Chem. Soc.* **1988**, *110*, 7980−7984.
(16) Xie, M.; Shen, Z.; Wang, D.; Fujii, A.; Lee, Y.-P. Spectral characterization of three-electron two-center (3e−2c) bonds of gaseous CH_3 ∴$S(H)CH_3$ and $(CH_3SH)_2^+$and enhancement of the 3e−2c bond upon protonation. *J. Phys. Chem. Lett.* **2018**, *9*, 3725−3730.
(17) Drewello, T.; Lebrilla, C. B.; Schwarz, H.; de Koning, L. J.; Fokkens, R. H.; Nibbering, N. M. M.; Anklam, E.; Asmus, K.-D. Formation of a two-centre, three-electron, sulphur−sulphur bond in the gas phase. *J. Chem. Soc., Chem. Commun.* **1987**, *0*, 1381−1383.
(18) Moradi, C. P.; Xie, C.; Kaufmann, M.; Guo, H.; Douberly, G. E. Two-center three-electron bonding in $ClNH_3$ revealed via helium droplet infrared laser Stark spectroscopy: Entrance channel complex along the Cl + NH_3 → $ClNH_2$ + H reaction. *J. Chem. Phys.* **2016**, *144*, 164301−164308.
(19) Zhang, S.; Wang, X.; Su, Y.; Qiu, Y.; Zhang, Z.; Wang, X. Isolation and reversible dimerization of a selenium−selenium three-electron σ-bond. *Nat. Commun.* **2014**, *5*, 1−7.
(20) Jie, J.; Xia, Y.; Huang, C.; Zhao, H.; Yang, C.; Liu, K.; Song, D.; Zhu, B.; Su, H. Sulfur-centered hemi-bond radicals as active intermediates in S-DNA phosphorothioate oxidation. *Nucleic Acids Res.* **2019**, *47*, 11514−11526.
(21) Vassilev, P.; Louwerse, M. J.; Baerends, E. J. Ab initio molecular dynamics simulation of the $OH^•$ radical in liquid water. *Chem. Phys. Lett.* **2004**, *398*, 212−216.
(22) Vassilev, P.; Louwerse, M. J.; Baerends, E. J. Hydroxyl radical and hydroxide ion in liquid water: A comparative electron density functional study. *J. Phys. Chem. B* **2005**, *109*, 23605−23610.
(23) Khalack, J. M.; Lyubartsev, A. P. Solvation structure of hydroxyl radical by Car-Parrinello molecular dynamics. *J. Phys. Chem. A* **2005**, *109*, 378−386.
(24) Svishchev, I. M.; Plugatyr, A. Y. Hydroxyl radical in aqueous solution: Computer simulation. *J. Phys. Chem. B* **2005**, *109*, 4123−4128.
(25) VandeVondele, J.; Sprik, M. A molecular dynamics study of the hydroxyl radical in solution applying self-interaction-corrected density functional methods. *Phys. Chem. Chem. Phys.* **2005**, *7*, 1363−1367.
(26) Braïda, B.; Hiberty, P. C.; Savin, A. A systematic failing of current density functionals: Overestimation of two-center three-electron bonding energies. *J. Phys. Chem. A* **1998**, *102*, 7872−7877.
(27) Kim, M.-C.; Sim, E.; Burke, K. Ions in solution: Density corrected density functional theory (DC-DFT). *J. Chem. Phys.* **2014**, *140*, 18A528.
(28) Codorniu-Hernández, E.; Kusalik, P. G. Insights into the solvation and mobility of the hydroxyl radical in aqueous solution. *J. Chem. Theory Comput.* **2011**, *7*, 3725−3732.
(29) Codorniu-Hernández, E.; Kusalik, P. G. Mobility mechanism of hydroxyl radicals in aqueous solution via hydrogen transfer. *J. Am. Chem. Soc.* **2012**, *134*, 532−538.
(30) Codorniu-Hernández, E.; Kusalik, P. G. Hydroxyl radicals in ice: Insights into local structure and dynamics. *Phys. Chem. Chem. Phys.* **2012**, *14*, 11639−11650.
(31) Codorniu-Hernández, E.; Boese, A. D.; Kusalik, P. G. The hemibond as an alternative condensed phase structure for the hydroxyl radical. *Can. J. Chem.* **2013**, *91*, 544−551.
(32) Kjellsson, L.; Nanda, K. D.; Rubensson, J.-E.; Doumy, G.; Southworth, S. H.; Ho, P. J.; March, A. M.; Al Haddad, A.; Kumagai, Y.; Tu, M.-F.; Schaller, R. D.; Debnath, T.; Bin Mohd Yusof, M. S.; Arnold, C.; Schlotter, W. F.; Moeller, S.; Coslovich, G.; Koralek, J. D.; Minitti, M. P.; Vidal, M. L.; Simon, M.; Santra, R.; Loh, Z.-H.; Coriani, S.; Krylov, A. I.; Young, L. Resonant inelastic x-ray scattering reveals hidden local transitions of the aqueous OH radical. *Phys. Rev. Lett.* **2020**, *124*, 236001.
(33) von Rudorff, G. F.; Jakobsen, R.; Rosso, K. M.; Blumberger, J. Improving the performance of hybrid functional-based molecular dynamics simulation through screening of Hartree−Fock exchange forces. *J. Chem. Theory Comput.* **2017**, *13*, 2178−2184.
(34) Apostolidou, C. OH radical in water from *ab initio* molecular dynamics simulation employing hybrid functionals. *J. Chem. Phys.* **2019**, *151*, 064111.
(35) Apostolidou, C. Vibrational spectra of the OH radical in water: Ab initio molecular dynamics simulations and quantum chemical calculations using hybrid functionals. *Adv. Theory Simul.* **2020**, *3*, 2000174.
(36) Adamo, C.; Barone, V. Toward reliable density functional methods without adjustable parameters: The PBE0 model. *J. Chem. Phys.* **1999**, *110*, 6158−6170.
(37) Grimme, S.; Antony, J.; Ehrlich, S.; Krieg, H. A consistent and accurate *ab initio* parameterization of density functional dispersion correction (DFT-D) for the 94 elements H−Pu. *J. Chem. Phys.* **2010**, *132*, 154104.
(38) Rana, B.; Herbert, J. M. Role of hemibonding in the structure and ultraviolet spectroscopy of the aqueous hydroxyl radical. *Phys. Chem. Chem. Phys.* **2020**, *22*, 27829−27844.
(39) Genova, A.; Ceresoli, D.; Pavanello, M. Avoiding fractional electrons in subsystem DFT based *ab-initio* molecular dynamics yields accurate models for liquid water and solvated OH radical. *J. Chem. Phys.* **2016**, *144*, 234105.
(40) Tsai, M.-K.; Kowalski, K.; Valiev, M.; Dupuis, M. Signature OH absorption spectrum from cluster models of solvation: A solvent-to-solute charge transfer state. *J. Phys. Chem. A* **2007**, *111*, 10478−10482.
(41) Chipman, D. M. Absorption spectrum of OH radical in water. *J. Phys. Chem. A* **2008**, *112*, 13372−13381.
(42) Chipman, D. M. Hemibonding between hydroxyl radical and water. *J. Phys. Chem. A* **2011**, *115*, 1161−1171.
(43) Chipman, D. M. Hemibonding between water cation and water. *J. Phys. Chem. A* **2016**, *120*, 9618−9624.
(44) Hoffman, G. J.; Gurunathan, P. K.; Francisco, J. S.; Slipchenko, L. V. Excited states of OH-$(H_2O)_n$ clusters for n = 1−4: An *ab initio* study. *J. Chem. Phys.* **2014**, *141*, 104315.
(45) Thomas, J. K.; Rabani, J.; Matheson, M. S.; Hart, E. J.; Gordon, S. Absorption spectrum of the hydroxyl radical. *J. Phys. Chem.* **1966**, *70*, 2409−2410.
(46) Boyle, J. W.; Ghormley, J. A.; Hochanadel, C. J.; Riley, J. F. Production of hydrated electrons by flash photolysis of liquid water with light in the first continuum. *J. Phys. Chem.* **1969**, *73*, 2886−2890.
(47) Pagsberg, P.; Christensen, H.; Rabani, J.; Nilsson, G.; Fenger, J.; Nielsen, S. O. Far-ultraviolet spectra of hydrogen and hydroxyl radicals from pulse radiolysis of aqueous solutions. Direct measurement of the rate of H + H. *J. Phys. Chem.* **1969**, *73*, 1029−1038.
(48) Treinin, A.; Hayon, E. Charge transfer spectra of halogen atoms in water. Correlation of the electronic transition energies of iodine, bromine, chlorine, hydroxyl, and hydrogen radicals with their electron affinities. *J. Am. Chem. Soc.* **1975**, *97*, 1716−1721.
(49) Nielsen, S. O.; Michael, B. D.; Hart, E. J. Ultraviolet absorption spectra of e_{aq}^-, H, OH, D, and OD from pulse radiolysis of aqueous solutions. *J. Phys. Chem.* **1976**, *80*, 2482−2488.
(50) Czapski, G.; Bielski, B. H. J. Absorption spectra of the $^•$OH and $O^{•-}$ radicals in aqueous solutions. *Radiat. Phys. Chem.* **1993**, *41*, 503−505.

https://doi.org/10.1021/acs.jpclett.1c02283
J. Phys. Chem. Lett. 2021, 12, 8053−8060

(51) Oldenberg, O.; Rieke, F. F. Kinetics of OH radicals as determined by their absorption spectrum III. A quantitative test for free OH; probabilities of transition. *J. Chem. Phys.* **1938**, *6*, 439−447.
(52) Pellerin, S.; Cormier, J. M.; Richard, F.; Musiol, K.; Chapelle, J. A spectroscopic diagnostic method using UV OH band spectrum. *J. Phys. D: Appl. Phys.* **1996**, *29*, 726.
(53) Gillan, M. J.; Alfè, D.; Michaelides, A. Perspective: How good is DFT for water? *J. Chem. Phys.* **2016**, *144*, 130901.
(54) Del Ben, M.; Hutter, J.; VandeVondele, J. Probing the structural and dynamical properties of liquid water with models including non-local electron correlation. *J. Chem. Phys.* **2015**, *143*, 054506.
(55) Reinhardt, A.; Cheng, B. Quantum-mechanical exploration of the phase diagram of water. *Nat. Commun.* **2021**, *12*, 1−7.
(56) Stillinger, F. H. *Energy Landscapes, Inherent Structures, and Condensed-Matter Phenomena;* Princeton University Press: Princeton, NJ, 2016.
(57) Niu, Z.; Tang, M.; Ge, N. Structure, stability, infrared spectra, and bonding of $OH^m(H_2O)_7$ (m = 0, ± 1) clusters: *Ab initio* study combining the particle swarm optimization algorithm. *Phys. Chem. Chem. Phys.* **2020**, *22*, 26487−26501.
(58) Jacobson, L. D.; Herbert, J. M. A one-electron model for the aqueous electron that includes many-body electron-water polarization: Bulk equilibrium structure, vertical electron binding energy, and optical absorption spectrum. *J. Chem. Phys.* **2010**, *133*, 154506.
(59) Jacquemin, D.; Adamo, C. Computational molecular electronic spectroscopy with TD-DFT. In *Density-Functional Methods for Excited States*; Ferré, N., Filatov, M., Eds.; Springer: Switzerland, 2016; Vol. *368*, pp 347−376.
(60) Elliott, P.; Furche, F.; Burke, K. Excited states from time-dependent density functional theory. In *Reviews in Computational Chemistry*; Lipkowitz, K. B., Cundari, T. R., Eds.; Wiley-VCH: New York, 2009; Vol. *26*, Chapter 3, pp 91−165.
(61) Laurent, A. D.; Jacquemin, D. TD-DFT benchmarks: A review. *Int. J. Quantum Chem.* **2013**, *113*, 2019−2039.
(62) Lange, A.; Herbert, J. M. Simple methods to reduce charge-transfer contamination in time-dependent density-functional calculations of clusters and liquids. *J. Chem. Theory Comput.* **2007**, *3*, 1680−1690.
(63) Lange, A. W.; Rohrdanz, M. A.; Herbert, J. M. Charge-transfer excited states in a π-stacked adenine dimer, as predicted using long-range-corrected time-dependent density functional theory. *J. Phys. Chem. B* **2008**, *112*, 6304−6308; *Erratum: J. Phys. Chem. B* **2008**, *112*, 7345.
(64) Isborn, C. M.; Mar, B. D.; Curchod, B. F. E.; Tavernelli, I.; Martínez, T. J. The charge transfer problem in density functional theory calculations of aqueously solvated molecules. *J. Phys. Chem. B* **2013**, *117*, 12189−12201.
(65) Carter-Fenk, K.; Mundy, C. J.; Herbert, J. M. Natural charge-transfer analysis: Eliminating spurious charge-transfer states in time-dependent density functional theory via diabatization, with application to projection-based embedding. *J. Chem. Theory Comput.* **2021**, *17*, 4195−4210.
(66) Magyar, R. J.; Tretiak, S. Dependence of spurious charge-transfer excited states on orbital exchange in TDDFT: Large molecules and clusters. *J. Chem. Theory Comput.* **2007**, *3*, 976−987.
(67) Lange, A. W.; Herbert, J. M. A smooth, nonsingular, and faithful discretization scheme for polarizable continuum models: The switching/Gaussian approach. *J. Chem. Phys.* **2010**, *133*, 244111.
(68) Pacchioni, G.; Frigoli, F.; Ricci, D.; Weil, J. A. Theoretical description of hole localization in a quartz Al center: The importance of exact electron exchange. *Phys. Rev. B: Condens. Matter Mater. Phys.* **2000**, *63*, 054102.
(69) Lægsgaard, J.; Stokbro, K. Hole trapping at Al impurities in silica: A challenge for density functional theories. *Phys. Rev. Lett.* **2001**, *86*, 2834−2837.
(70) To, J.; Sokol, A. A.; French, S. A.; Kaltsoyannis, N.; Catlow, C. R. A. Hole localization in $[AlO_4]^0$ defects in silica materials. *J. Chem. Phys.* **2005**, *122*, 144704.
(71) Liao, P.; Carter, E. A. Hole transport in pure and doped hematite. *J. Appl. Phys.* **2012**, *112*, 013701.
(72) Ansari, N.; Ulman, K.; Camellone, M. F.; Seriani, N.; Gebauer, R.; Piccinin, S. Hole localization in Fe_2O_3 from density functional theory and wave-function-based methods. *Phys. Rev. Mater.* **2017**, *1*, 035404.
(73) Zawadzki, P.; Rossmeisl, J.; Jacobsen, K. W. Electronic hole transfer in rutile and anatase TiO_2: Effect of a delocalization error in the density functional theory on the charge transfer barrier height. *Phys. Rev. B: Condens. Matter Mater. Phys.* **2011**, *84*, 121203R.
(74) Elmaslmane, A. R.; Watkins, M. B.; McKenna, K. P. First-principles modeling of polaron formation in TiO_2 polymorphs. *J. Chem. Theory Comput.* **2018**, *14*, 3740−3751.
(75) Liu, T.; Cui, M.; Dupuis, M. Hole polaron transport in bismuth vanadate $BiVO_4$ from hybrid density functional theory. *J. Phys. Chem. C* **2020**, *124*, 23038−23044.
(76) Ohio Supercomputer Center; http://osc.edu/ark:/19495/f5s1ph73 (accessed 2021-08-12).

https://doi.org/10.1021/acs.jpclett.1c02283
J. Phys. Chem. Lett. 2021, 12, 8053−8060